IEEE Access
Multidisciplinary | Rapid Review | Open Access Journal

Received November 19, 2018, accepted December 18, 2018, date of publication December 24, 2018,
date of current version January 16, 2019.

Digital Object Identifier 10.1109/ACCESS.2018.2889245

Development of Modular Cable-Driven Parallel Robotic Systems

SEN QIAN, BIN ZI, DAOMING WANG, AND YUAN LI
School of Mechanical Engineering, Hefei University of Technology, Hefei 230009, China

Corresponding author: Bin Zi (binzi.cumt@163.com)

This work was supported by the National Natural Science Foundation of China under Grant 51575150 and Grant 51605126.

ABSTRACT Task-oriented modular design and safety monitoring are demonstrated to be outstanding challenges for robots in practical application. In order to obtain better flexibility and better obstacles avoidance capability, design and analysis of a modular cable-driven parallel robot (MCDPR) are presented in this paper, which can be reconfigured to several configurations in engineering applications by changing the number of the mobile modules and the connection mode of the end effector. With regard to the motion control and safety monitoring system, the design and implementation of hardware and software are presented. An experimental prototype for the MCDPR is developed, followed by a brief illustration of the connection mode between the end effector and cables, and the installation of monitoring nodes. The performance of the MCDPR is discussed experimentally, including real-time pose monitoring and obstacle avoidance. The results verify the feasibility and efficiency of kinematics model and obstacle avoidance method, and the results also indicate that the designed motion control and safety monitoring system can realize trajectory tracking control, real-time safety monitoring, and obstacle avoidance for the MCDPR.

INDEX TERMS Cable-driven parallel robots, design and implementation, safety monitoring, obstacle avoidance.

I. INTRODUCTION

In the last decade, cable-driven parallel robots (CDPRs) have attracted a considerable amount of interest owing to a wide area of applications and a lot of advantages, including large reachable workspace, high acceleration capability and economical construction [1]–[3]. In CDPR, flexible cables are applied in place of rigid-link legs to support and manipulate the end-actuator [4]. Due to these advantages, the CDPRs are eligible for applications like video capture system [5], large spherical radio telescope [6], large scale 3D printer [7], removing graffiti from highway signs [8], cooperative crane system [9], periodic maintenance of suspension bridge [10], humanoid robotic arm and musculoskeletal system [11], [12], and robot rehabilitation [13], [14]. All these CDPRs have made valuable contributions to mechanical behavior and mechatronics technology of the robotics. However, according to specific applications, most of them are concentrated on a single operational task of the CDPRs [15].

More recently, the realm of the CDPRs is beginning to manifest its advantages, and high performance operation with high payload and great flexibility is an important task in modern engineering applications [6]–[9], [16], [17]. Thus, under this situation, to meet the performance requirements in terms of multifunction, high precision and reliability, payload-to-weight ratio for the CDPRs, it is necessary to explore the modular design of the task-oriented compound-driven CDPRs and safety monitoring system of complex electromechanical system. Modular robots have received more and more attention to meet the requirement of flexibility in the manufacturing industry [18]–[21].

CDPRs offer many advantages considering the flexibility of cables. However, cables can only actuate unilaterally through tension, which limits the moment resisting and exerting capabilities. Research in the topic of modular CDPRs (MCDPR) is highly motivated, which can enhance the orientation workspaces of CDPRs and overcome the drawback of CDPRs, especially the collisions between the cables and the surrounding Environment [22]–[24]. Modular design enables modular CDPRs to change their module and size to meet specific operational demands and possess broad application prospects. For instance, multiple mobile cranes, as shown in Fig. 1, can be used for material transportation, weight elevation, steel erection and roof installation, etc. The cooperative lifting system consists of three and even more cranes can be seen as the possible applications of MCDPR by changing the number of the mobile cranes and the connection

FIGURE 1. Applications of multiple mobile cranes.

mode of payload. In order to obtain better flexibility and obstacles avoidance capability, design and analysis of the MCDPR are presented in this paper, which can be reconfigured to several configurations of CDPRs in engineering applications by changing the number of the mobile modules and the connection mode of end-effector. After addressing the design issue, understanding and evaluating the mechanical behavior of the MCDPR is important for heterogeneous tasks in different environments. Kinematics plays an important role in manipulator behavior. Kinematic analysis has been relatively presented in the work on manipulator robots [25], [26].

Safety of the CDPRs is the important consideration before it can be materialized. A number of studies investigate the design and implementation of system monitoring, safety strategy for human-robot collaboration system, and reliability and safety of robot systems [27]–[30]. Consequently, it is critical that only dependable robot monitoring systems are deployed for human-robot collaborative tasks. Safety is the unified criterion for future technical challenges in the design and control of human-robot systems. However, mechanical structures and physical characteristics of the CDPRs can hardly meet safe requirements absolutely and carry a high risk of injuries to operators. Additionally, in consideration of unpredictable obstacles within the operation environment, obstacle avoidance proves to be a pressing problem that must be solved for safety consideration [16].

The primary motivation of this study is to investigate the design, safety monitoring, and obstacle avoidance of the MCDPR in order to meet the performance requirements in terms of multifunction, high reliability and payload-to-weight ratio for the CDPRs. The contribution includes three aspects. (1) A MCDPR is designed for better flexibility and better obstacles avoidance capability, which can be reconfigured to several configurations by changing the number of the mobile modules and the connection mode of end-effector. (2) Mechatronic hardware and software for the experimental testbed are carried out with regard to the motion control and safety monitoring system. (3) The effectiveness of the safety monitoring and obstacle avoidance is verified through experimental studies. This paper is organized as follows. Section II introduces the issues involved in the system description of the MCDPR. The hardware and software implementation of the motion control and safety monitoring system is provided in Section III. Section IV describes the development of the experimental testbed. The performances of the MCDPR are evaluated and discussed in Section V. Finally, conclusions are given in Section VI.

II. SYSTEM DESCRIPTION

Referring to Fig. 2, the MCDPR can be reconfigured to several configurations to imitate different types of RCDPR in engineering applications by changing the number of the mobile modules and the connection mode of end-effector. With four typical configurations shown in Fig. 2, the MCDPR are mainly consisted by a circular orbit, six groups of CDPRs, six flexible cables and an end-effector. More specifically, six mobile modules are equipped on a circular orbit. They can rotate along a circular trajectory with respect to the center line of the orbit through gear transmission driven by a servomotor. A cable drum and a hydraulic cylinder with a fix pulley at the top are both installed on each individual mobile module. The pulley component is freely rotatable about the vertical axis of the cylinder. For each cable, one end is rolled in a drum, and the other end is directed to the end-effector through a pulley. The end-effector, employed as a controlled object, is actuated by the cables to manipulate all DOFs.

Obviously in Fig. 2, configuration I and III illustrates three-cable and four-cable point-mass CDPRs which is underconstrained. Configurations II and IV are respectively the three-cable and four-cable underconstrained CDPRs. Configuration V shows underconstrained CDPRs with six DOFs. Configuration VI shows underconstrained CDPRs with three translational degree of freedom actuated by three parallel cable groups and a rotating degree of freedom around vertical direction actuated by mobile modules. Moreover, the vertical stretch of the hydraulic cylinder and the rotation of the mobile module along the circular orbit can also alter configuration parameters of the MCDPR to improve flexibility and save costs for optimization [19].

III. DESIGN OF MOTION CONTROL AND SAFETY MONITORING SYSTEM

A. MOTION CONTROL SYSTEM

Fig. 3 shows the hardware of the motion control system, which is composed of an industrial personal computer (IPC), a motion controller, a pinboard and several servomotors and drivers.

Basic mechanism and kinematic parameters should be configured prior to system startup. Specific values of parameters are determined through measurements. After parameter configuration, the control system starts up and the host computer starts to upload the configuration data, eliminate the alarm information, set the motion mode of the shaft and switch on the enabler for servomotors. Then, the motion module planning is performed based on the motion mode selection

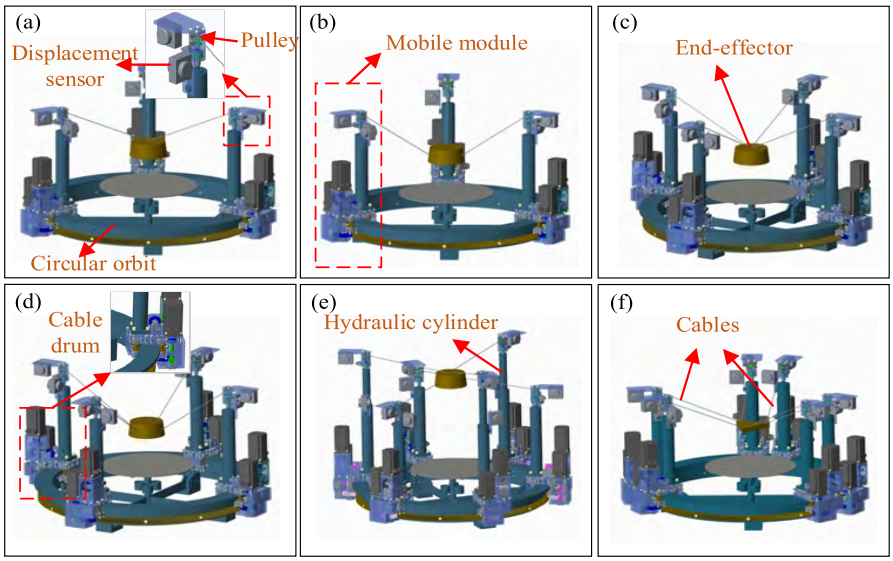

FIGURE 2. Several typical configurations of MCDPR: (a) configuration I; (b) configuration II; (c) configuration III; (d) configuration IV; (e) configuration V; (f) configuration VI.

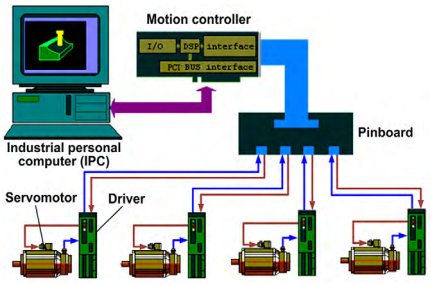

FIGURE 3. Hardware configuration of the motion control system.

after motor initialization. The motion mode typically contains the straight line mode and the spiral line mode. After motor position planning, the curves severed as the motor input immediately plot in the software interface. Thereafter, the motor stops upon the termination of the planning. Note that a reset process is needed because the end-effector offsets its original pose after an experiment.

The host computer interface for the motion control system is designed as depicted in Fig. 4. It contains seven modules, which are respectively the basic mechanism parameter configuration module, the mode selection module, the kinematic parameter configuration module, the mechanism display module, the system startup and stop module, the planning curve display module, as well as the motor position planning module.

B. SAFETY MONITORING SYSTEM

The MCDPR is designed for payload hoisting. As described in the introduction, the cooperative lifting system consists of three and even more cranes can be seen as the possible applications of the MCDPR with different configurations, which is a typical human-robot system. In the development of human-robot systems, safety is the unified criterion for future technical challenges. However, mechanical structures and physical characteristics of the CDPRs can hardly meet the safe requirements, which will cause severe injuries to humans. Thus it is important to develop a monitoring system to avoid collision and keep the security of operators through sensors and signal processing techniques.

1) HARDWARE IMPLEMENTATION

Fig. 5 shows the hardware structure of the safety monitoring system, which includes master control module, sensor module, wireless transmission module and power source module. The master control module, responsible for data operation, storage and power consumption management, is the core of the hardware system. A single chip micyoco (SCM) is selected as the microprocessor for master control module. Additionally, the sensors for obstacle monitoring and end-effector pose monitoring, choose infrared obstacle avoidance (IOA) sensor and displacement sensor, respectively. For the wireless transmission module, a radio frequency chip with a carrier frequency of 433 Hz is used for the data forwarding from monitoring nodes to sink nodes. The power source module is in charge of the power supply for all the other modules. A rechargeable Li-ion battery is a good candidate due to its compact size, long endurance and large capacity.

The monitoring circuit board includes the master control module and the power module. For circuit diagram design of the master control module, it contains the model selection of microprocessor and the peripheral circuit design. The power source module is used as a power supply for the circuit board and the wireless module. The working voltage of the circuit board and sensor module is 5V while that of the wireless module is 3.3V.

2) SOFTWARE IMPLEMENTATION

The software structure of the safety monitoring system is presented in Fig. 6. There are three steps from data acquisition to data processing listed as:

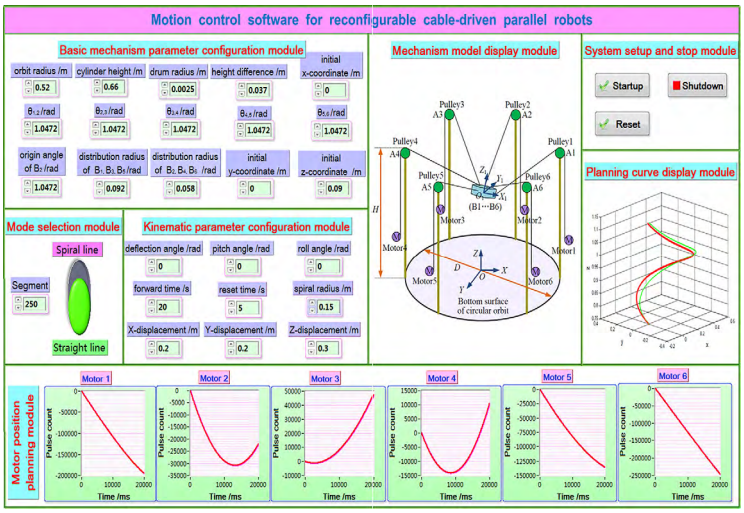

FIGURE 4. Host computer interface for motion control system.

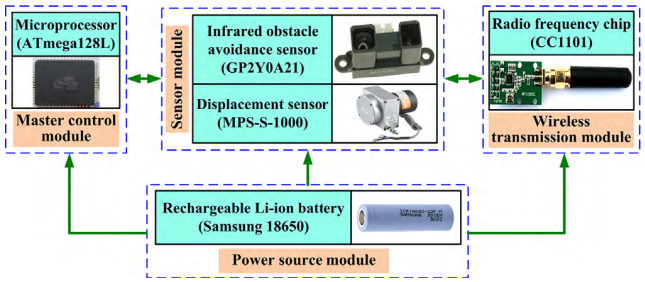

FIGURE 5. Hardware structure of safety monitoring system.

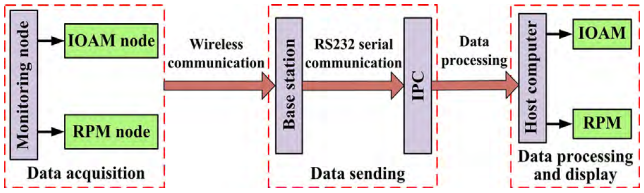

FIGURE 6. Software structure of safety monitoring system.

Step 1 (Data Acquisition): The monitoring node is divided into the IOA monitoring (IOAM) node and the real-time pose monitoring (RPM) node. They are separately applied for the monitoring of obstacle position, as well as the cable length and the calculated real-time pose of the end-effector.

Step 2 (Data Sending): The wireless transmission method can overcome the shortcomings compared with the traditional wire communication method, such as cockamamie wiring and environmental sensitive. Firstly, the raw data is sent to the base station through wireless communication, and then it is forwarded to the IPC through RS232 serial communication.

Step 3 (Data Processing and Display): The data packet analysis is conducted by the host computer to gain required data for each module. Specifically, the data from IOA sensors is converted to acquire the real-time position of obstacles. Therefore, the data is able to display directly on the host computer. As for the real-time pose data, it is obtained through the forward kinematic solution based on the feedback cable length.

As is known to us, it is not allowed for any people or object to emerge in the workspace of the end-effector during operation in case of accidents. The designed IOAM functional module can achieve the RPM of obstacles and send the monitoring data to the host computer.

The IOA sensor (GP2Y0A21) is adopted to identify whether there is obstacle in front of the sensor. The effective range and angle of IOA are 80cm and 40°, respectively. The resolution of IOA is 50 μm. The output signal of the sensor has a direct nonlinear relation with the distance in the range from 0 to 10cm while an inverse nonlinear relation with the distance from 10 to 80cm. The orbit radius is 60cm which falls within range from 10 to 80cm. However, the measuring range of 0∼10cm can be regarded as a blind area because it locates in the orbit edge far away from the end-effector. Thus, the area can be considered as a relative safe area. Actually, eight IOA sensors are used to achieve a full-scale monitoring of 360° since the effective measuring range of a single sensor is greater than 45°.

The correspondence between output voltage and sensing distance of IOA sensor is calibrated through several measurements, as shown in Fig. 7. The relationship curve in the distance range from 10 to 80cm can be approximately treated as six short straight lines. Accordingly, the relation between output voltage (U_{out}) and sensing distance (d) follows the expression as

$$\begin{cases} \text{Line A: } d = -8.33(U_{\text{out}} - 1.7) + 15 & U_{\text{out}} \geq 1.7 \\ \text{Line B: } d = -12.5(U_{\text{out}} - 1.3) + 20 & 1.3 \leq U_{\text{out}} < 1.7 \\ \text{Line C: } d = -25.2(U_{\text{out}} - 0.9) + 30 & 0.9 \leq U_{\text{out}} < 1.3 \\ \text{Line D: } d = -50.5(U_{\text{out}} - 0.7) + 40 & 0.7 \leq U_{\text{out}} < 0.9 \\ \text{Line E: } d = -80.5(U_{\text{out}} - 0.5) + 60 & 0.5 \leq U_{\text{out}} < 0.7 \\ \text{Line F: } d \approx 80 \rightarrow \text{No obstacle} & U_{\text{out}} < 0.5 \end{cases} \quad (1)$$

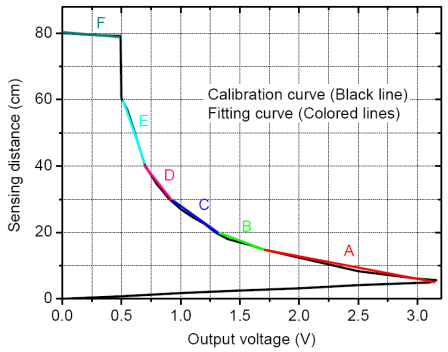

FIGURE 7. Correspondence between output voltage and sensing distance.

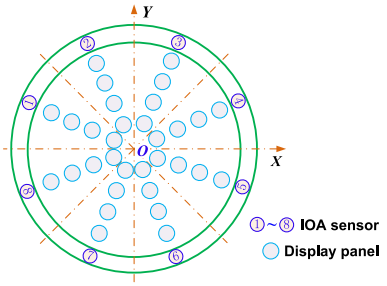

FIGURE 8. Layout of infrared sensors and display panels.

According to the data packet from IOA sensors, the obstacle information at a specific node is obtained after converting output voltage into sensing distance. The layout of infrared sensors and display panels are depicted in Fig. 8. It shows that eight sensors are arranged uniformly along the orbit. In addition, four circular display panels are positioned along the radial direction for each sensor, corresponding respectively to four regions of 0∼15cm, 15∼30cm, 30∼45cm and 45∼60cm. Once the distance between the obstacle and the node reduces to a certain value, the corresponding panel changes its color immediately which denotes obstacles in the area.

The RPM functional module is to acquire the real-time pose of the end-effector through the aforementioned forward kinematic solution of the monitoring data from six displacement sensors. The theoretical trajectory of the end-effector displays in the host computer interface for the convenient check and comparison by operators. Any program that satisfies MATLAB language specifications can be written into the internal of the script node. Then, the motion mode planning is accomplished through definitions of input and output parameters.

IV. EXPERIMENTAL TESTBED

Fig. 9 shows physically the experimental testbed for the MCDPR. A hydraulic pump with a supply power of only 1MPa is used for the stretch of the hydraulic cylinder. The outlet of the pump is connected to six valve blocks and each block is connected in series with a cut-off valve, a pilot-controlled check valve and a direct-acting proportional valve. During the experiments, the lifting speed of the cylinder is adjusted by controlling the opening size of the proportional valve with a proportional amplifier. Two servomotors are installed on each mobile module for the rotation of the mobile module around the circular orbit and the rotation of the cable drum.

TABLE 1. Main configuration parameters of the testbed.

Object	Parameter	Symbol	Value
Circular orbit	Radius	R_o	0.52m
End-effector	Mass	M_e	20kg
	Radius	R_e	0.1m
	Thickness	H_e	0.05m
Cylinder	Height	H_c	0.66m
Obstacle	Length×Width×Height	L×W×H	0.04m×0.16m×0.255m

A rectangular obstacle is located on the platform. The cable drum is utilized for the wrapping of the cable through a fix pulley to elevate the end-effector. Main configuration parameters of the testbed is given in Table 1. A specific illustration of the connection mode between cables and the end-effector is presented in Fig. 10 for both RPM and IOAM experiments. In Fig. 10(a), three connection joints B2, B4, B6 are distributed evenly on the top surface of the end-effector with a distribution radius of Ru = 75mm.

Meanwhile, the other three connection joints are distributed evenly on the medial diagonal plane of the side circle with a distribution radius of Rd = 125mm. The rotational angle between cable 2 and cable 1 is $\pi/6$. As for the connection mode for IOAM experiment, three cables, numbered 1, 3, 5, are distributed evenly along circumferential direction and they are all connected to a point B which locates just above the center of the top surface of the end-effector.

Referring to the hardware design of monitoring system in Section IV, the monitoring nodes are divided into IOAM node and RPM node. A picture that illustrates the installation of these monitoring nodes is presented in Fig. 11.

1) IOAM node. An infrared sensor GP2Y0A21 is installed at the IOAM node which is fixed on the outside surface of the mobile module. Additionally, the sensor is installed right in front of the workspace.

2) RPM node. A displacement sensor MPS-S-1000 is installed at the RPM node, specifically in the front side of the pulley. The sensor wire, fixed by a U-shaped plate and a pulley bracket, is guaranteed to be parallel to the cable. The signal output port of the sensor is accessed to the RPM node through a wire pinboard.

V. PERFORMANCE EVALUATION AND DISCUSSION

A. REAL-TIME POSE MONITORING

1) FORWARD KINEMATIC SOLUTION

The forward kinematic solution of MCDPR refers to the solution of the spatial pose for end-effector with known cable length changes. Fig. 12 illustrates the schematic of a

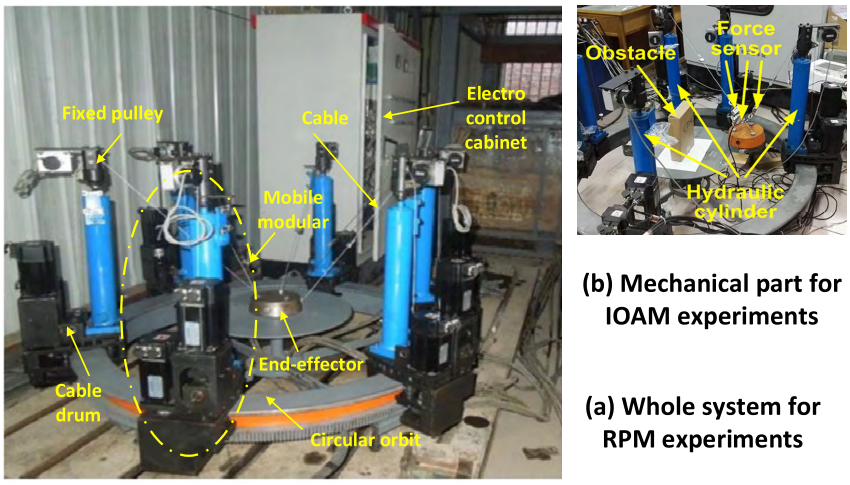

FIGURE 9. Picture of the experimental testbed for MCDPR.

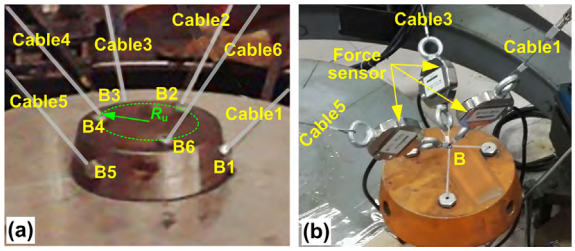

FIGURE 10. Connection modes between cables and end-effector for (a) RPM experiment; (b) IOAM experiment.

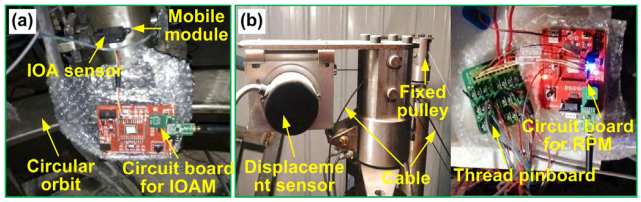

FIGURE 11. Installation of monitoring nodes: (a) IOAM node, (b) RPM node.

6 cable-driven parallel mechanism. The real-time end-effector pose is regulated by changing the cable lengths through the control of corresponding motors, which can subsequently realize a high-accuracy spatial motion of the end-effector. Two coordinate systems, the global coordinate system $OXYZ$ and the local coordinate system $O_1X_1Y_1Z_1$, are established before the derivation of kinematic equations. As depicted in Fig. 12, the origin of $OXYZ$ locates in the orbit center on the ground while that of $O_1X_1Y_1Z_1$ in the end-effector center. The end-effector has six DOFs with its spatial pose described by the origin coordinates of $O_1X_1Y_1Z_1$ (x, y, z), and the rotation angles of the end-effector around X, Y and Z axes (α, β, γ). In which, x, y, z separately denote X-coordinate, Y-coordinate and Z-coordinate, and α, β, γ are deflection angle, pitch angle and roll angle, respectively.

The sagging of cable should be taken into account when establishing the accurate model of the cable

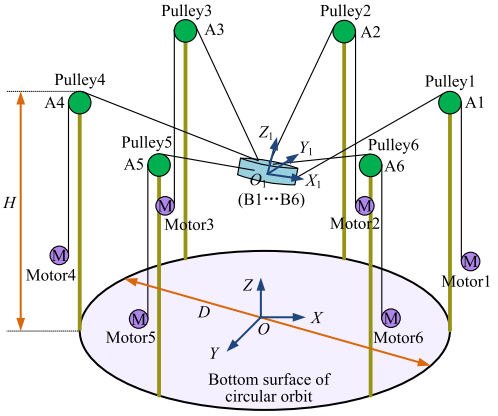

FIGURE 12. Schematic of a 6 cable-driven parallel mechanism.

parallel robot [31]. However, in order to ensure the real-time performance, the flexibility of the cable is neglected for simplicity, which is treated as a massless body.

The Jacobian matrix describes the linear relation between the velocities of six cables and end-effector [32], which can be expressed as

$$\dot{\boldsymbol{L}} = \boldsymbol{J} \cdot \dot{\boldsymbol{S}} \tag{2}$$

$\dot{\boldsymbol{S}}$ is the end-effector velocity, which can be presented as

$$\dot{\boldsymbol{S}} = [\dot{x} \quad \dot{y} \quad \dot{z} \quad \dot{\alpha} \quad \dot{\beta} \quad \dot{\gamma}]^{\mathrm{T}} \tag{3}$$

$\dot{\boldsymbol{L}}$ is the velocities of six cables given by the representation

$$\dot{\boldsymbol{L}} = \left[\dot{L}_1 \quad \dot{L}_2 \quad \dot{L}_3 \quad \dot{L}_4 \quad \dot{L}_5 \quad \dot{L}_6\right]^{\mathrm{T}} \tag{4}$$

$\boldsymbol{J}$ refers to a 6×6 Jacobian matrix that relates to the spatial velocity of the end-effector

$$\boldsymbol{J} = \left[\frac{\partial L_i}{\partial x} \quad \frac{\partial L_i}{\partial y} \quad \frac{\partial L_i}{\partial z} \quad \frac{\partial L_i}{\partial \alpha} \quad \frac{\partial L_i}{\partial \beta} \quad \frac{\partial L_i}{\partial \gamma}\right]^{\mathrm{T}} \tag{5}$$

Following variables are defined for simplification

$(s \triangleq \sin, c \triangleq \cos)$

$$\begin{cases} X_{i1} = x_{\mathrm{A}i} - x_{\mathrm{B}i} \\ Y_{i1} = y_{\mathrm{A}i} - y_{\mathrm{B}i} \\ Z_{i1} = z_{\mathrm{A}i} - z_{\mathrm{B}i} \end{cases} \tag{6}$$

$$\begin{cases} X_{i2} = -c\beta s\gamma x_{1\mathrm{B}i} - c\beta c\gamma y_{1\mathrm{B}i} \\ X_{i3} = -s\beta c\gamma x_{1\mathrm{B}i} + s\beta s\gamma y_{1\mathrm{B}i} + c\beta z_{1\mathrm{B}i} \end{cases} \tag{7}$$

$$\begin{cases} Y_{i2} = (c\beta s\gamma - s\alpha s\beta \mathrm{S}\gamma)x_{1\mathrm{B}i} - (c\beta s\gamma + s\alpha s\beta c\gamma)y_{1\mathrm{B}i} \\ Y_{i3} = s\alpha c\beta c\gamma x_{1\mathrm{B}i} - s\alpha c\beta s\gamma y_{1\mathrm{B}i} + s\alpha s\beta z_{1\mathrm{B}i} \\ Y_{i4} = (c\alpha s\beta c\gamma - s\alpha s\gamma)x_{1\mathrm{B}i} \\ \qquad - (c\alpha c\gamma + c\alpha s\beta s\gamma)y_{1\mathrm{B}i} - c\alpha c\beta z_{1\mathrm{B}i} \end{cases} \tag{8}$$

$$\begin{cases} Z_{i2} = (s\alpha c\gamma + c\alpha s\beta s\gamma)x_{1\mathrm{B}i} - (s\alpha s\gamma - c\alpha s\beta c\gamma)y_{1\mathrm{B}i} \\ Z_{i3} = c\alpha c\beta c\gamma x_{1\mathrm{B}i} + c\alpha c\beta s\gamma y_{1\mathrm{B}i} - c\alpha s\beta z_{1\mathrm{B}i} \\ Z_{i4} = (c\alpha s\gamma + s\alpha s\beta c\gamma)x_{1\mathrm{B}i} \\ \qquad + (c\alpha c\gamma - s\alpha s\beta s\gamma)y_{1\mathrm{B}i} - s\alpha c\beta z_{1\mathrm{B}i} \end{cases} \tag{9}$$

where $(x_{\mathrm{A}i}, y_{\mathrm{A}i}, z_{\mathrm{A}i})$ and $(x_{\mathrm{B}i}, y_{\mathrm{B}i}, z_{\mathrm{B}i})$ are the coordinates of Ai and Bi in the global coordinate system $OXYZ$, $(x_{1\mathrm{B}i}, y_{1\mathrm{B}i}, z_{1\mathrm{B}i})$ are the coordinates of Bi in the local coordinate system $O_1X_1Y_1Z_1$.

Then, the expression of each element in the kinematic Jacobian matrix is derived as

$$\begin{cases} \partial L_i/\partial x = X_{i1}/L_i \\ \partial L_i/\partial y = Y_{i1}/L_i \\ \partial L_i/\partial z = Z_{i1}/L_i \\ \partial L_i/\partial \alpha = (X_{i1}X_{i2} + Y_{i1}Y_{i2} + Z_{i1}Z_{i2})/L_i \\ \partial L_i/\partial \beta = (X_{i1}X_{i3} + Y_{i1}Y_{i3} + Z_{i1}Z_{i3})/L_i \\ \partial L_i/\partial \gamma = (Y_{i1}Y_{i4} + Z_{i1}Z_{i4})/L_i \end{cases} \tag{10}$$

The end effector moves along the trajectory from initial pose in the workspace through changing the cable length. The real-time length vector of each cable is symbolized as $\boldsymbol{L}$. Theoretically, $\boldsymbol{P}_0$, the initial pose vector of the end-effector, is possible to choose any spatial pose. In this study, the forward kinematic solution of MCDPR can be simplified to the current pose solution of the end-effector according to $\boldsymbol{P}_0$ and $\boldsymbol{L}$. Fig. 13 summarizes the flow chart of the numeric-based algorithm for forward pose solution.

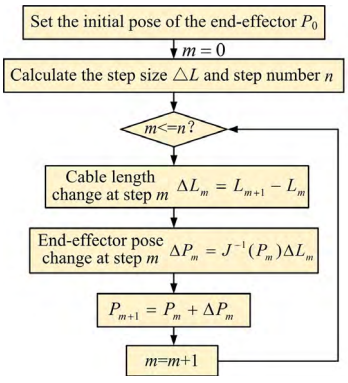

FIGURE 13. Numeric-based algorithm for forward pose solution.

On the basis of the algorithm shown in Fig. 13, kinematics is simulated using MATLAB software. The desired end-effector trajectory is defined as the following equations

$$\begin{cases} x = 0.25 - 0.25\cos(\pi t/2) \\ y = 0.25\sin(\pi t/2) \\ z = 0.1t + 0.75 \\ \alpha = \pi t/24 \\ \beta = \pi t/24 \\ \gamma = \pi t/48 \end{cases} \quad (0 \le t \le 4) \tag{11}$$

where t represents time.

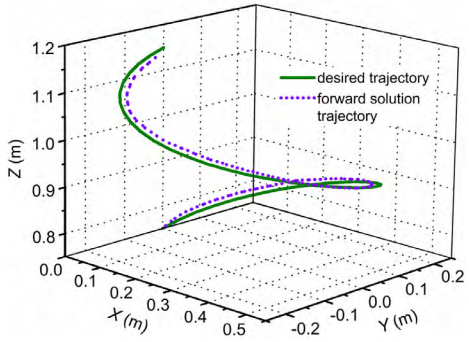

FIGURE 14. Desired trajectory and forward solution trajectory for end-effector.

A comparison of desired trajectory and forward solution trajectory is obtained as illustrated in Fig. 14. The end-effector trajectory is donated to be a rising spiral line. Moreover, the changing trends of two trajectories are essentially coincident and the max range of error is 0.005m, which in return validates the feasibility of utilizing the numeric-based solution algorithm for the forward kinematic solution of MCDPR.

2) RPM EXPERIMENTS

In RPM experiments, the motion mode is assigned to be vertical lifting motion. X, Y and Z displacements are separately 0m, 0.25m and 0m. Deflection angles of three axes are all 0. Fig. 15 displays a comparison of theoretical length and actual length for six cables. The variations of cable length with time are presented to be substantial agreement with each other for six cables. Meantime, a slight fluctuation is still found in the measured curves due to the inadequate system stiffness, along with the vibration induced by flexible characteristics associated with cables.

Referring to the comparison of theoretical and measured trajectory shown in Fig. 16, when the end effector moving in the Z direction, the measured trajectory fits the theoretical trajectory with good accuracy (see Fig.16 (c)). However, the increased tension and the resulted elastic extension of cables during the movement cause wild movements of the values in X direction, Y direction and three pose angles, including deflection angle, pitch angle and roll angle. A detailed illustration of the pose deviation for the end-effector is given in Table 2.

As for the absolute displacement deviations in X, Y and Z directions, the maximum values are 0.03959m, 0.04544m

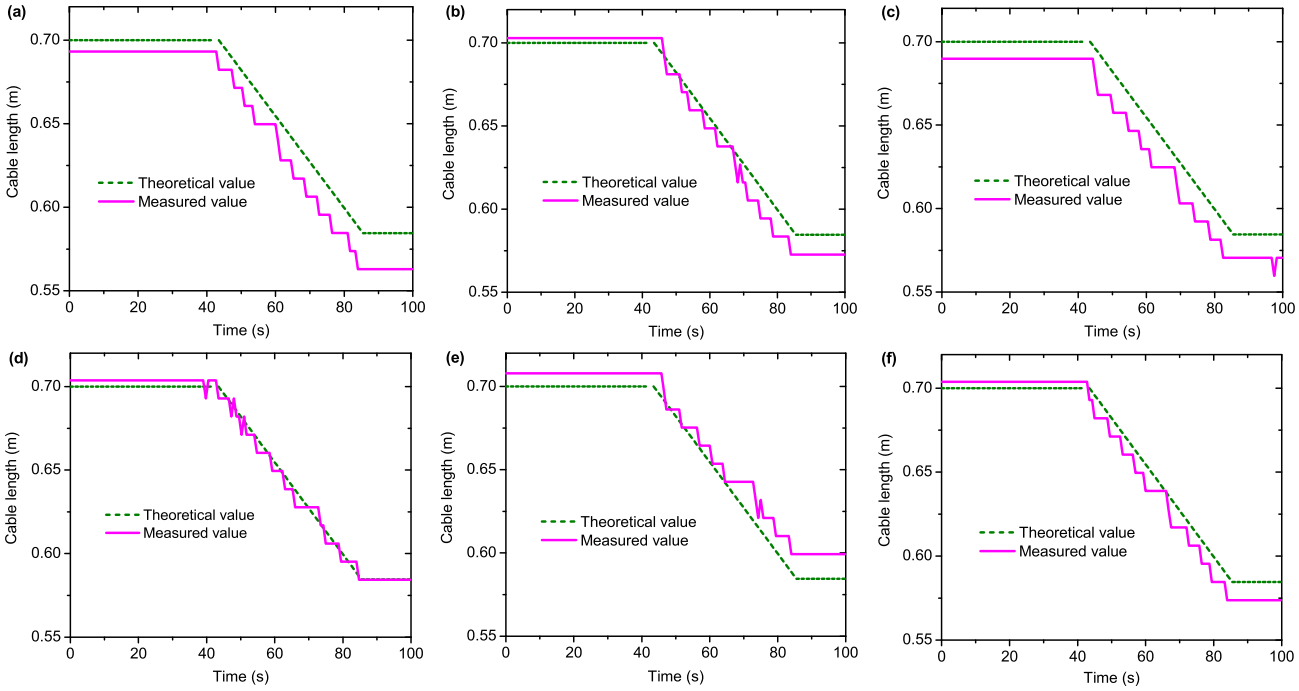

FIGURE 15. Theoretical length and actual length for six cables: (a) cable 1, (b) cable 2, (c) cable 3, (d) cable 4, (e) cable 5, (f) cable 6.

TABLE 2. Pose deviation of the end-effector.

Parameter	Absolute Deviation	
	Maximum	Average
X-displacement (m)	0.03959	0.01624
Y-displacement (m)	0.04544	0.01719
Z-displacement (m)	0.01781	0.00796
Deflection angle (°)	2.408	1.091
Pitch angle (°)	3.825	1.628
Roll angle (°)	8.236	3.954

and 0.00796m while the average values are only 0.01624m, 0.01719m, respectively. Furthermore, the average deviations of deflection angle, pitch angle and roll angle are 1.091o, 1.628o and 3.954o, respectively. The end-effector trajectory tracking error is caused by different error sources, including kinematic error, deformation and servo error. Kinematic error caused by machining, assembly and operation is the major error sources, including the influence of force sensors and pulleys on the kinematics [33]–[35]. Note that these deviations can be eliminated by the purposed robust iterative learning controller in [9]. Thus, the end-effector can be elevated smoothly within the accepted error range.

B. OBSTACLE AVOIDANCE

1) THEORETICAL MODEL

As seen in Fig. 2, the RCDPR can change their module and size to meet specific operational demands for the simulation of the task-oriented cooperative work of 3 to 6 mobile modules. In this study, the 3 modules type configuration shown in Fig. 2a, which is widely used in engineering applications, is chosen for the cooperative operation analysis. The schematic of the MCDPR for configuration I is shown in Fig. 17.

The end-effector is simplified to be a mass point with its coordinates to be (X_B, Y_B, Z_B) in the global coordinate system *OXYZ*. Then, the coordinate vector of the end point B are described by

$$\boldsymbol{B} = (X_B,\ Y_B,\ Z_B) \tag{12}$$

The coordinate vector for three top ends A1-A3 is given as

$$\boldsymbol{A}_i = (R_o\cos(\theta_i),\ R_o\sin(\theta_i),\ h_i) \quad (i = 1, 2, 3) \tag{13}$$

where θ_i is the rotational angle of the *i*th mobile module.

Hence, based on the inverse kinematic model in [3]. The length of *i*th cable is derived as

$$L_i = \sqrt{(X_B - R_o\cos(\theta_i))^2 + (Y_B - R_o\sin(\theta_i))^2 + (Z_B - h_i)^2} \quad (i = 1,\ 2, 3) \tag{14}$$

Due to the configuration, the static mechanical model of the end-effector is expressed by

$$\sum_{i=1}^{3} F_i \cdot \frac{\overrightarrow{A_iB}}{\left\|\overrightarrow{A_iB}\right\|} = M_e g \tag{15}$$

where F_i is the tension force of *i*th cable. for other configurations, static mechanical model can be derived similarly.

Since the cable can only provide tension force and it is guaranteed not to be loosened during operation, then

$$F_{max} \geq F_i \geq F_{min} \tag{16}$$

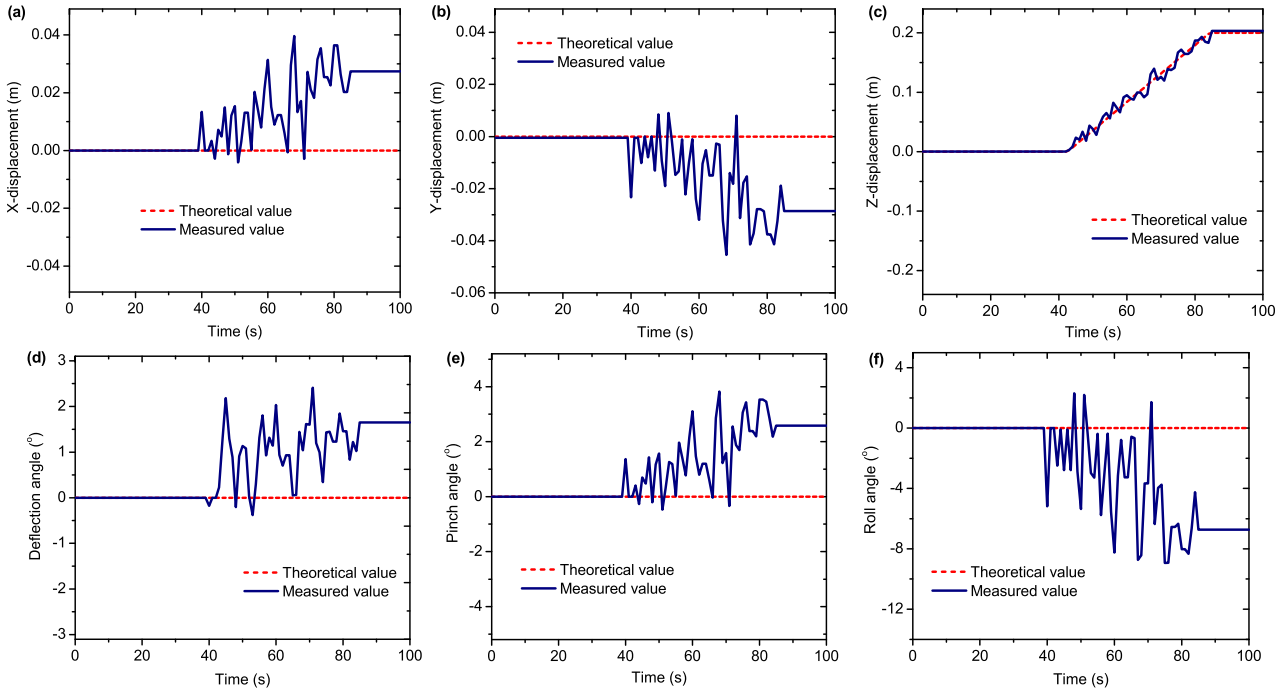

FIGURE 16. Theoretical trajectory and measured trajectory for the end-effector: (a) X-displacement, (b) Y-displacement, (c) Z-displacement, (d) deflection angle, (e) pitch angle, (f) roll angle.

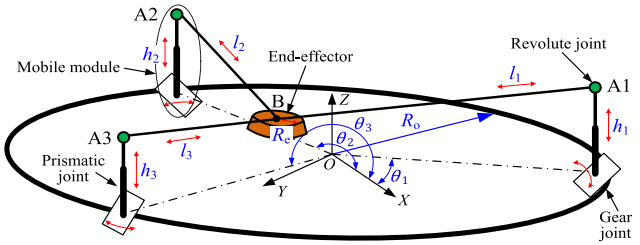

FIGURE 17. Schematic of the MCDPR for configuration I.

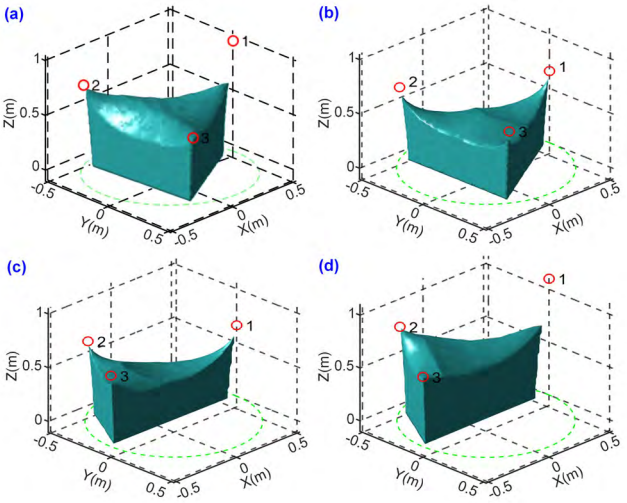

FIGURE 18. Workspaces for various cylinder heights and rotational angles: (a).

where $F_{\max}$ and $F_{\min}$ are respectively the maximum and minimum tension forces.

Based on the aforementioned static mechanical model of the MCDPR (configuration I), the workspace calculation is carried out with following parameters given as $F_{\max} = M_{\mathrm{e}}\mathrm{g}$, $F_{\min} = 0$. The results for various cylinder heights h_i and rotational angles θ_i are obtained as depicted in Fig. 18. The workspace can be approximately regarded as a triangle formed by three mobile modules. In addition, the volumes of the workspaces are calculated as 0.1293, 0.1713, 0.0882 and 0.1138m^3 for different conditions shown in Fig. 18(a) to (d), respectively.

Fig. 19 is the simplified top view of the RCDPR, where the gray polygons represent the workspace formed by several mobile modules. Both the end-effector and cables need to avoid collisions with obstacles during operation. For the end-effector, its trajectory can easily obtained by using the artificial potential field method, which is widely adopted for obstacle avoidance in engineering practice. The environment is treated as a potential field where the combinations of attraction and repulsion elements are used to represent the destination and obstacles, respectively. Continuous and smooth motion is obtained with closed-form expressions of the trajectory velocity. During the end-effector moving along the given trajectory, all these cables need to avoid collisions with obstacles. As three mobile modules locates at the initial position A1-A2-A3 and the end-effector moves from the start point S to the goal point G, cable 3 (line PA3) is inevitably collide with the obstacle. To prevent

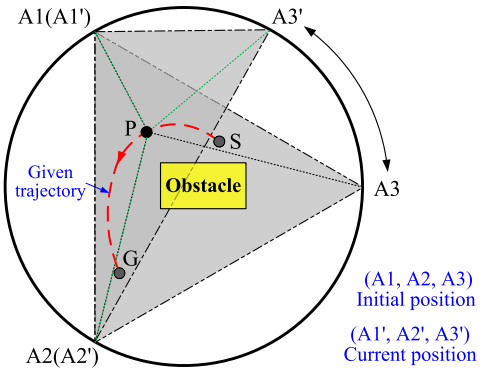

FIGURE 19. Sketch of the obstacle avoidance process.

this, three mobile modules can be reconfigured to the position A1′-A2′-A3′. Now, both the cables and end-effector are able to avoid collisions with the obstacle

To identify the position to ensure each mobile modules can move without collisions, the anchor point of each cable is assumed to be a ''light source''. And the arc that formed by the cast shadow of the obstacle is perceived as the forbidden area of the corresponding mobile module. As shown in Fig.20, the anchor point of each cable is coincide with each other, so the read dashed arc is the common forbidden area of these three mobile module. For other type of configurations, the forbidden area of each mobile module need to be calculated, respectively.

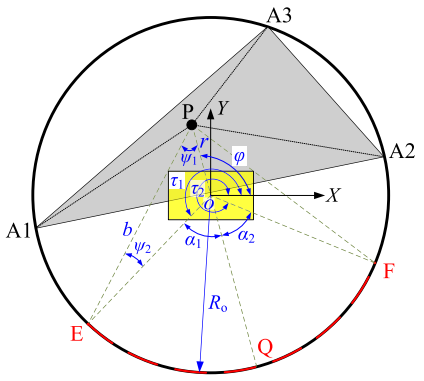

FIGURE 20. Schematic of the obstacle avoidance algorithm.

In Fig. 20, r represents the distance between an arbitrary point P on the trajectory and the origin point O. E and F are two boundary points of the obstacle projection on the orbit closed to mobile module 1 and mobile module 2, respectively. Q is the intersection point between the extended line PO and the orbit. Here, $\angle POX = \varphi$, $\angle EPQ = \psi_1$, $\angle PEO = \psi_2$, $\angle EOQ = \alpha_1$, $\angle QOF = \alpha_2$. Once the coordinate of P is given, the value of ψ_1 and φ can be calculated using the coordinates of P and obstacle corners. Then, α_1 can be calculated using

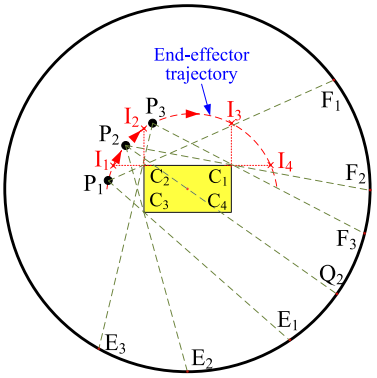

FIGURE 21. Abrupt change positions of boundary points.

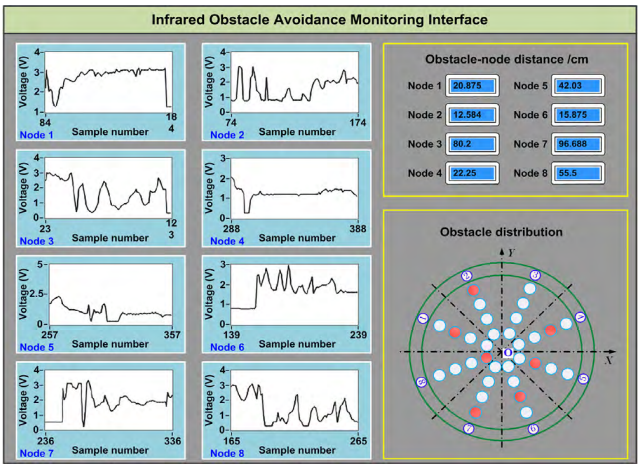

FIGURE 22. Real-time display interface of IOAM.

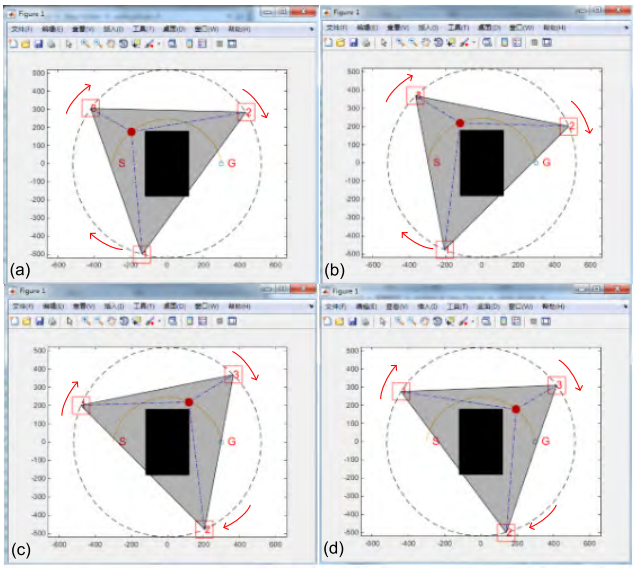

FIGURE 23. Simulation results at four abrupt change positions: (a) I_1; (b) I_2; (c) I_3; (d) I_4.

the formula below

$$\begin{cases} \cos\psi_1 = \left(b^2 + r^2 - R_o^2\right)/2br \\ \psi_2 = \arccos\left[\left(b^2 + R_o^2 - r^2\right)/2bR_o\right] \\ \alpha_1 = \psi_1 + \psi_2 \end{cases} \tag{17}$$

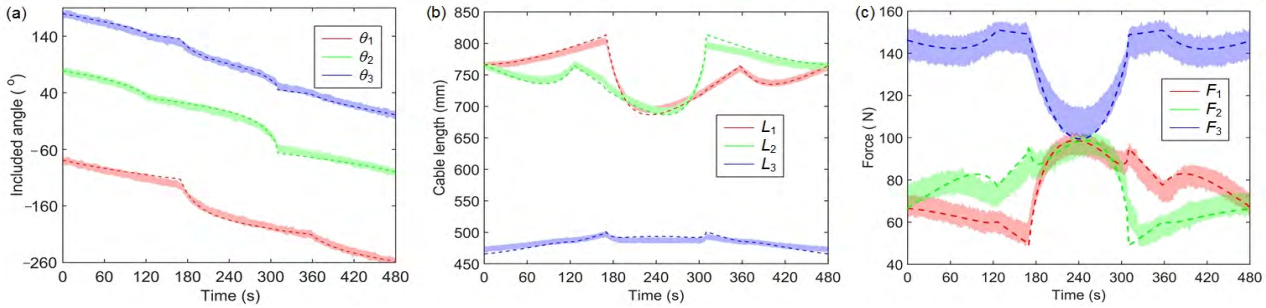

FIGURE 24. A comparison of simulation results and experimental data: (a) rotational angle; (b) cable length; (c) force.

where b is the distance between the arbitrary point P and boundary point E. The value of α_2 can be obtained using the above approach similarly.

The rotational angles between line OE, line OF and X-axis are symbolized as τ_1, and τ_2 with their values obtained as $\tau_1 = \varphi + \pi - \alpha_1$ and $\tau_2 = \varphi + \pi + \alpha_2$. Then, the positions of two boundary points of the inferior arc can also be solved.

Here a buffer angle η is employed to reduce the risk of collision between cables and the obstacle, the position angles θ_i between mobile module 1, 2, 3 and X-axis are set as

$$\begin{cases} \theta_1 = \tau_1 - \eta \\ \theta_2 = \tau_2 + \eta \\ \theta_3 = \theta_1 + \theta_2 \end{cases} \tag{18}$$

Note that the position angles θ_3 is set to be the average value of θ_1 and θ_2 to make cable force evenly distributed. For other type of configurations, the position angles θ_i of each mobile module can be obtained similarly.

Theoretically, an abrupt change in the positions of boundary points E, F may appear when the end-effector pass over the intersection points between the trajectory and the extensions of obstacle edges. As shown in Fig. 21, when the end-effector moves from P_1 to I_1 then to P_2, the pivot of boundary line PF switches from C_2 to C_1, causing an abrupt change in the motion gain of the end-effector. Moreover, the boundary line between line PQ and the movement direction of the end-effector switches its pivot firstly at each obstacle corner. In the figure, I_1 and I_3 are the abrupt change positions of F, I_2 and I_4 are the abrupt change positions of E. Note that a constant safe angle is used to avoid collision, as seen in (18), the abrupt change of boundary points will directly reflect in the movement of the mobile module.

2) SIMULATION AND EXPERIMENT OF IOAM

The IOAM node can monitor the real-time position of obstacles placed arbitrarily in the workspace. The display interface of IOAM is plotted in Fig. 22. In the figure, the obstacle distribution sub-interface is intended for the real-time visualization of the approximate position of obstacles. Simultaneously, the exact obstacle position in the radial direction is available from the obstacle-node distance sub-interface. Note that the sampling period is 0.01s in the experiments.

Simulation and experiment of obstacle-avoidance for the MCDPR are conducted sequentially with the parameters below: Initial end-effector position is (−0.3m, 0, 0.25m), terminal end-effector position is (0.3m, 0, 0.25m), and cylinder height are $h_1 = h_2 = h_3 = 0.66$m. The values of rotational angles θ_1, θ_2, θ_3 are solved by substituting the end-effector trajectory into (17) and (18), which obtained via the artificial potential field method [36]. The movement process of the MCDPR utilized the obstacle avoidance algorithm is simulated and the results at four abrupt change positions are displayed in Fig. 23. The results indicate that the MCDPR can effectively achieve obstacle-avoidance after reconfiguration by rapidly changing the circumferential position of the mobile module at abrupt change positions.

Fig. 24 shows the variations of rotational angle, cable length and force with time of simulation and experiment. In the figure, the solid line donates the experimental data while the dot line represents the simulation results. Two inflection points are found on the curves of both θ_1 and θ_2, corresponding separately to the moment of four abrupt change positions shown in Fig. 23. In specific, mobile modules 1, 2 abruptly alter their circumferential positions at 170s, 355s, and 125s, 310s. Moreover, the curves of θ_1 and θ_2 are symmetric due to the symmetry of the rectangular obstacle and the interchangeability between mobile modules 1 and 2. Similarly, the symmetry and inflection points also appear in the curves of θ_3 and subsequent cable length L_i and force F_i. In addition, the variation trend of experimental results are in good agreement with the simulation values. However, due to the kinematic error sources, measurement error and the acceleration neglected in the static mechanical model, there are some differences between the results of experiment and simulation, particularly at inflection points.

VI. CONCLUSIONS

In this paper, design, safety monitoring, and obstacle avoidance for the MCDPR is presented to meet the performance requirements in terms of multifunction and payload-to-weight ratio for the CDPRs. Modular design and system description of the MCDPR were presented. The paper detailed the hardware and software implementations of the system. The kinematics of the MCDPR is analyzed using

forward solution method and the theoretical model for obstacle avoidance of the MCDPR with three DOFs was derived. Two categories of experiments were conducted, including the real-time pose monitoring and obstacle avoidance. For the pose deviation of the end-effector, the mean values were 0.01624m and 0.01719m in X and Y directions while that in Z direction was rather small, only 0.00796m. Simultaneously, the average deviations of deflection angle, pinch angle and roll angle were 1.091°, 1.628° and 3.954°, respectively. In the obstacle avoidance experiments, mobile modules 1, 2 abruptly alter their circumferential positions at 170s, 355s, and 125s, 310s, which leads to corresponding inflections of rotational angle, cable length and force. Additionally, the curves of cable length and force appear symmetrically with respect to the time midpoint due to the symmetry of the rectangular obstacle and the interchangeability between mobile modules.

Experimental results confirmed the feasibility and efficiency of the kinematics model and obstacle avoidance method. The motion control and safety monitoring system were proved to be effective for realization of real-time safety monitoring and obstacle avoidance of the MCDPR. Future work will focus on efficient reconfiguration strategies of MCDPR for better performance and flexibility in cluttered environment, by determining the optimal number of the mobile modules and locations of the cable anchor points.

REFERENCES

[1] S. H. Yeo, G. Yang, and W. B. Lim, "Design and analysis of cable-driven manipulators with variable stiffness," *Mechanism Mach. Theory*, vol. 69, pp. 230–244, Nov. 2013.
[2] B. Zi and S. Qian, *Design, Analysis and Control of Cable-Suspended Parallel Robots and Its Applications*. Singapore: Springer, 2017.
[3] B. Zi and Y. Li, "Conclusions in theory and practice for advancing the applications of cable-driven mechanisms," *Chin. J. Mech. Eng.*, vol. 30, no. 4, pp. 763–765, 2017.
[4] Y. Wang, G. Yang, T. Zheng, K. Yang, and D. Lau, "Force-closure workspace analysis for modular cable-driven manipulators with co-shared driving cables," in *Proc. 13th IEEE Conf. Ind. Electron. Appl. (ICIEA)*, May/Jun. 2018, pp. 1504–1509.
[5] C. Gosselin and S. Foucault, "Dynamic point-to-point trajectory planning of a two-DOF cable-suspended parallel robot," *IEEE Trans. Robot.*, vol. 30, no. 3, pp. 728–736, Jun. 2014.
[6] B. Y. Duan, Y. Y. Qiu, F. S. Zhang, and B. Zi, "On design and experiment of the feed cable-suspended structure for super antenna," *Mechatronics*, vol. 19, no. 4, pp. 503–509, 2009.
[7] B. Zi, N. Wang, S. Qian, and K. Bao, "Design, stiffness analysis and experimental study of a cable-driven parallel 3D printer," *Mechanism Mach. Theory*, vol. 132, pp. 207–222, Feb. 2019.
[8] S. P. Donohoe, S. A. Velinsky, and T. A. Lasky, "Mechatronic implementation of a force optimal underconstrained planar cable robot," *IEEE/ASME Trans. Mechatronics*, vol. 21, no. 1, pp. 69–78, Feb. 2016.
[9] S. Qian, B. Zi, and H. Ding, "Dynamics and trajectory tracking control of cooperative multiple mobile cranes," *Nonlinear Dyn.*, vol. 83, nos. 1–2, pp. 89–108, Jan. 2016.
[10] K. H. Cho *et al.*, "Inspection robot for hanger cable of suspension bridge: Mechanism design and analysis," *IEEE/ASME Trans. Mechatronics*, vol. 18, no. 6, pp. 1665–1674, Dec. 2013.
[11] Q. Chen, W. Chen, G. Yang, and R. Liu, "An integrated two-level self-calibration method for a cable-driven humanoid arm," *IEEE Trans. Autom. Sci. Eng.*, vol. 10, no. 2, pp. 380–391, Apr. 2013.
[12] H. Kino, S. Kikuchi, Y. Matsutani, K. Tahara, and T. Nishiyama, "Numerical analysis of feedforward position control for non-pulley musculoskeletal system: A case study of muscular arrangements of a two-link planar system with six muscles," *Adv. Robot.*, vol. 27, no. 16, pp. 1235–1248, 2013.
[13] Y. Mao and S. K. Agrawal, "Design of a cable-driven arm exoskeleton (CAREX) for NEURAL rehabilitation," *IEEE Trans. Robot.*, vol. 28, no. 4, pp. 922–931, Aug. 2012.
[14] P. K. Jamwal, S. Q. Xie, S. Hussain, and J. G. Parsons, "An adaptive wearable parallel robot for the treatment of ankle injuries," *IEEE/ASME Trans. Mechatronics*, vol. 19, no. 1, pp. 64–75, Feb. 2014.
[15] B. Zi, H. Sun, and D. Zhang, "Design, analysis and control of a winding hybrid-driven cable parallel manipulator," *Robot. Comput.-Integr. Manuf.*, vol. 48, pp. 196–208, Dec. 2017.
[16] B. Zi, J. Lin, and S. Qian, "Localization, obstacle avoidance planning and control of a cooperative cable parallel robot for multiple mobile cranes," *Robot. Comput.-Integr. Manuf.*, vol. 34, pp. 105–123, Aug. 2015.
[17] S. Qian, B. Zi, W.-W. Shang, and Q. Xu, "A review on cable-driven parallel robots," *Chin. J. Mech. Eng.*, vol. 31, p. 66, Dec. 2018.
[18] G. Rosati, D. Zanotto, and S. K. Agrawal, "On the design of adaptive cable-driven systems," *J. Mech. Robot.*, vol. 3, no. 2, p. 021004, 2011.
[19] X. Zhou, C. P. Tang, and V. Krovi, "Analysis framework for cooperating mobile cable robots," in *Proc. IEEE Int. Conf. Robot. Automat.*, vol. 20, May 2012, pp. 3128–3133.
[20] L. Gagliardini, S. Caro, M. Gouttefarde, and A. Girin, "Discrete reconfiguration planning for cable-driven parallel robots," *Mechanism Mach. Theory*, vol. 100, pp. 313–337, Jun. 2016.
[21] S. Abdolshah, D. Zanotto, G. Rosati, and S. K. Agrawal, "Optimizing stiffness and dexterity of planar adaptive cable-driven parallel robots," *J. Mech. Robot.*, vol. 9, no. 3, p. 031004, 2017.
[22] J. Lin, C. S. Huang, and J. Chang, "A mechatronic kit with a control methodology for a modualized cable-suspended robot," *J. Vib. Control*, vol. 22, no. 20, pp. 4211–4226, 2016.
[23] G. Castelli and E. Ottaviano, "Modelling and simulation of a cable-based parallel manipulator as an assisting device," in *Computational Kinematics*. Berlin, Germany: Springer, 2006, pp. 17–24.
[24] M. Anson, A. Alamdari, and V. Krovi, "Orientation workspace and stiffness optimization of cable-driven parallel manipulators with base mobility," *J. Mech. Robot.*, vol. 9, no. 3, p. 031011, 2017.
[25] G. Abbasnejad, J. Yoon, and H. Lee, "Optimum kinematic design of a planar cable-driven parallel robot with wrench-closure gait trajectory," *Mechanism Mach. Theory*, vol. 99, pp. 1–18, May 2016.
[26] A. Peidró, A. Gil, J. M. Marín, and Ó. Reinoso, "A Web-based tool to analyze the kinematics and singularities of parallel robots," *J. Intell. Robot. Syst.*, vol. 81, no. 1, pp. 145–163, 2016.
[27] B. S. Dhillon, A. R. M. Fashandi, and K. L. Liu, "Robot systems reliability and safety: A review," *J. Qual. Maintenance Eng.*, vol. 8, no. 3, pp. 170–212, 2002.
[28] J. T. C. Tan, F. Duan, R. Kato, and T. Arai, "Safety strategy for human–robot collaboration: Design and development in cellular manufacturing," *Adv. Robot.*, vol. 24, nos. 5–6, pp. 839–860, 2010.
[29] E. Cabal-Yepez, A. G. Garcia-Ramirez, R. J. Romero-Troncoso, A. Garcia-Perez, and R. A. Osornio-Rios, "Reconfigurable monitoring system for time-frequency analysis on industrial equipment through STFT and DWT," *IEEE Trans. Ind. Informat.*, vol. 9, no. 2, pp. 760–771, May 2013.
[30] N. Sun, Y. Fang, and H. Chen, "A continuous robust antiswing tracking control scheme for underactuated crane systems with experimental verification," *J. Dyn. Syst., Meas., Control*, vol. 138, no. 4, p. 041002, 2016.
[31] J.-P. Merlet and J. Alexandre-Dit-Sandretto, "The forward kinematics of cable-driven parallel robots with sagging cables," in *Cable-Driven Parallel Robots*. Cham, Switzerland: Springer, 2015, pp. 3–15.
[32] M. Carricato and J.-P. Merlet, "Stability analysis of underconstrained cable-driven parallel robots," *IEEE Trans. Robot.*, vol. 29, no. 1, pp. 288–296, Feb. 2013.
[33] E. Ottaviano, M. Ceccarelli, and F. Palmucci, "An application of CaTraSys, a cable-based parallel measuring system for an experimental characterization of human walking," *Robotica*, vol. 28, no. 1, pp. 119–133, 2010.
[34] A. Pott, "Influence of pulley kinematics on cable-driven parallel robots," *Latest Advances in Robot Kinematics*. Dordrecht, The Netherlands: Springer, 2012, pp. 197–204.
[35] A. Gonzalez-Rodriguez, F. J. Castillo-Garcia, E. Ottaviano, P. Rea, and A. G. Gonzalez-Rodriguez, "On the effects of the design of cable-Driven robots on kinematics and dynamics models accuracy," *Mechatronics*, vol. 43, pp. 18–27, May 2017.
[36] D. Lau, J. Eden, and D. Oetomo, "Fluid motion planner for nonholonomic 3-D mobile robots with kinematic constraints," *IEEE Trans. Robot.*, vol. 31, no. 6, pp. 1537–1547, Dec. 2015.

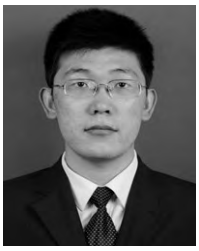

SEN QIAN received the Ph.D. degree from the China University of Mining and Technology, China, in 2015. He is currently a Lecturer with the School of Mechanical Engineering, Hefei University of Technology, China. His research interests include robotics and automation.

BIN ZI received the Ph.D. degree from Xidian University, China, in 2007. He is currently a Professor, the Dean of the School of Mechanical Engineering, and the Director of the Robotics Institute, Hefei University of Technology, China. His research interests include robotics and automation, mechatronics, and multirobot systems.

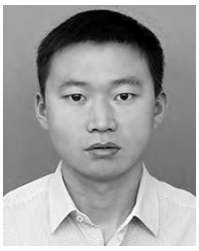

DAOMING WANG received the Ph.D. degree from the China University of Mining and Technology, China, in 2014. He is currently an Associate Professor with the School of Mechanical Engineering, Hefei University of Technology, China. His research interests include mechatronics and smart materials.

YUAN LI is currently pursuing the Ph.D. degree with the School of Mechanical Engineering, Hefei University of Technology, China.